Nanoscale

ARTICLE

Oxidative nucleation and growth of Janus-type MnOx-Ag and MnOx-AgI nanoparticles

Lei Zhang,[1,2] Lei Jin,[2] Yue Yang,[2,4] Peter Kerns,[2] Xingsong Su,[1,2] Michael Meng,[2] Ben Liu,[1,*] and Jie He[2,3,*]

Janus nanoparticles (NPs) containing two chemically distinct materials in one system are of great significance for catalysis in terms of harnessing catalytic synergies that are not exist in either component. We herein present a novel synthetic method of two Janus-type MnOx-Ag and MnOx-AgI NPs. The synthesis of Janus-type MnOx-AgI NPs is based on the oxidative nucleation and growth of Ag domains on MnO first and the subsequent iodization of Ag. A mild and non-disruptive iodization strategy is developed to yield Janus MnOx-AgI NPs, in which converting Ag to AgI domains with iodomethane (CH_3I) is achieved through the partial iodization. Simultaneously, Mn^{2+} species in the primary MnO octahedra are oxidized during the growth of Ag NPs, leading to the formation of amorphous p-type MnOx domains. Therefore, as-resultant Janus-type MnOx-AgI NPs combining two semiconductors into an integrated nanostructure can be used as an efficient photocatalyst for visible light-driven water oxidation. Janus MnOx-AgI NPs show an expected photocatalytic activity even in the absence of $Ru(bpy)_3Cl_2$ as an electron mediator. This intriguing synthesis may open up a new opportunity to develop asymmetric nanostructures of two semiconductors that will potentially be efficient photocatalysts for solar-driven water splitting.

Introduction

Rational design of multicomponent hybrid nanoparticles (NPs) with intrinsically disparate functionality has been of continuous interest for decades. The marriage of different components in one nanostructure, not only creates multifunctional materials to meet various requirements in a variety of applications, but also generate the synergetic properties that are not exist in individual components.[1] Tremendous effort has been made in the synthesis of hybrid nanostructures in different topologies, such as core/shell,[2,3] heterostructures (e.g., asymmetric nanostructures)[4,5] and alloys[6,7]. Among them, Janus-type NPs have been emerged as a new generation to effectively combine two distinct components together, which provides extraordinary capabilities to endow the dual functionalities to one NP.[8, 9]

Janus-type NPs which combine two chemically distinct materials (e.g., organic/inorganic hybrids[10] and metal/metal oxide) in one system are of particularly interest in the field of catalysis.[11,12] One example is the use of localized surface plasmon resonance of noble metal NPs (e.g., Ag and Au) to enhance the light harvesting of adjacent semiconductors through plasmon-coupled resonance energy transfer[13] and hot-electron injection. Janus-type TiO2-Au[12] or ZnO-Au[14,15] NPs that have shown higher activity for photocatalytical hydrogen generation compared to core-shell or physical mixture counterparts. Alternatively, Janus NPs consisting of two semiconductors can also greatly enhance the photocatalytic activity through broadening the absorption and/or effective charge separation at the interface of the two semiconductors. Janus-like MnS/Cu7S4 nanostructures as a Z-scheme system were reported to harvest solar light over a broad spectrum and dramatically improve the activity of photocatalytic hydrogen production.[16]

Mn based oxides are a p-type semiconductor as potentially interesting materials for hole conductivity. There are extensive literatures on the synthetic mimics of the nature photosynthesis using MnOx polymorphs for water oxidation reactions (WORs).[17-29] A few polymorphs of MnOx have the appropriate energy of valence band and a suitable band gap for solar-driven WORs, e.g., birnessite-type MnO2 with a band gap of ca. 1.8-2.3 eV.[30] The activity of synthetic photocatalysts for WORs is usually assessed using a $[Ru(bpy)_3]^{2+}/S_2O_8^{2-}$ system.[31] $[Ru(bpy)_3]^{2+}$ as an electron mediator can effectively separate the excited electrons from MnOx to drive the oxidation of water on MnOx. Despite numerous efforts being devoted to the new synthesis of asymmetric NPs, only very few successful examples are documented for MnOx-containing Janus NPs. The likely reason is that, the rich redox chemistry of Mn ($Mn^{2+} \rightarrow Mn^{3+} \rightarrow Mn^{4+}$) makes it extremely challenging to maintain the structural integrity of the MnOx domains during the growth of the second NPs.[32-35,36] One example from Tremel group is using heterogeneous nucleation of MnO on oleylamine-capped gold NPs

through the decomposition of the manganese oleate.[34] The favorable nucleation of MnO as Janus-type only coursed on the certain size of gold NPs and therefore limited the size control of Janus NPs. So far, no examples on the use of MnO as seeds to grow the second domain in the form of Janus-type have been reported.

Scheme 1. Synthetic strategy of Janus-type MnO_x-AgI NPs through an oxidative nucleation and growth of Ag on MnO octahedra and a mild iodization using CH_3I.

We herein present a new and robust method to prepare Janus-type MnO_x-Ag and MnO_x-AgI NPs using an oxidative nucleation and growth method. The growth of Janus-type MnO_x-Ag and MnO_x-AgI is based on a two-step controllable nucleation and subsequent iodination of Ag NPs on octahedral MnO NPs (Scheme 1). MnO octahedra prepared through thermal decomposition of $Mn(oleate)_2$ are used as seeds first to grow highly monodispersed Janus MnO_x-Ag NPs. Followed by a mild iodination of MnO_x-Ag NPs with CH_3I at room temperature, well-defined Janus MnO_x-AgI NPs can be prepared in remarkable yield and high homogeneity. Compared to KI and I_2 as an iodide source reported in previous literatures,[37,38] the iodination using CH_3I is none-disruptive to the nanostructures of Ag and this leads to the formation of spherical core-shell Ag@AgI (about 42 % iodination yield) in as-resultant MnO_x-AgI NPs. We show that Janus-type MnO_x-AgI NPs as photocatalysts are very active and reasonably stable for oxygen evolution in the solar-driven WORs. The photoactivity of MnO_x-AgI NPs shows a minimum dependence on the presence of $Ru(bpy)_3Cl_2$ as an electron mediator. The two examples of Janus-type MnO_x nanostructures illustrate a new avenue to develop MnO_x-containing asymmetric nanostructures, which are applicable in photocatalysis.

Results and discussion

The synthetic route of Janus-type MnO_x-AgI NPs is illustrated in Scheme 1. Octahedral MnO nanocrystals was first synthesized by thermal decomposition of $Mn(oleate)_2$ in the presence of excess oleic acid as capping agents using previously reported method.[39,40] As-prepared MnO nanocrystals were octahedral with a diameter of 15.0 ± 1.4 nm (Figures 1a, S1 and S3a). After the removal of excess oleic acid by centrifugation, MnO octahedra were dispersed in hexane. To this solution, $AgNO_3$ precursor dissolved in oleylamine was injected at room temperature and then heated to ~110 °C at a heating rate of 5 °C/min. The fast nucleation of Ag grains was indicated by the immediate color change from yellowish to dark brown. The reaction mixture was further refluxed for 1 h and purified by centrifugation.

Figures 1b-c and S2 display the typical TEM images of Janus-type MnO_x-Ag NPs. The formation of Janus-type nanostructures is in high yield and homogeneity. The size of MnO_x octahedra is 13.4 ± 1.8 nm (Figure S3b); while the diameter of Ag domains is 12.0 ± 2.2 nm (Figure S4a). The decrease in the size of MnO_x domains implies the possible leaching of Mn compared to the initial MnO octahedra. Under high-angle annular dark-field scanning transmission electron microscopy (HAADF-STEM, Figure 1d), it is interesting to point out that there are a number of ultrasmall Ag domains (around 1 nm) grown on MnO_x octahedra. Clear lattice is observed in the darker side of Janus nanostructures where the lattice distance was measured to be *ca.* 0.24 nm, corresponding to the *d*-spacing of (111) planes of Ag nanocrystals (Figure 1e). No obvious lattice of MnO was found on the octahedral (brighter) side; instead, smaller crystalline domains with barely measurable lattice were seen. It is indicative of the oxidative disruption of MnO octahedra to likely form MnO_x in a higher valence during the reduction of $AgNO_3$. This result was further confirmed by powder X-ray diffraction (XRD) of Janus MnO_x-Ag NPs and primary MnO octahedra (Figure 1f). Well-resolved diffraction peaks of MnO confirm its rack-salt crystal before the growth of Ag domains; while, all the diffraction peaks of MnO disappear for Janus MnO_x-Ag NPs, in which only a set of diffraction peaks from *fcc* Ag (JCPDF#4-783) were observed. Since Janus MnO_x-Ag NPs lost the crystallinity of initial MnO octahedra and produced completely amorphous MnO_x domains, an oxidative nucleation and growth of Ag likely occurred, in consistent with the analysis of STEM.

To better understand the growth mechanism of Janus-type MnO_x-Ag NPs, the evolution of MnO_x-Ag intermediates at different reaction times was investigated in detail using TEM (Figure S5). After introduction of $AgNO_3$ and oleylamine, heteronucleation of Ag on the surface of MnO octahedra was observed. These extremely small Ag grains (< 1 nm) grew simultaneously on the surface of MnO octahedra at the beginning of the reaction. After 5 min, a slightly bigger Ag domain (3.7 ± 0.8 nm) emerged at the edge or the corner of MnO octahedra, accompanying with randomly distributed small Ag grains over the surface of MnO octahedra (Figure S5a-b). Since MnO and Ag have distinct lattice parameters and surface energies, the fast heteronucleation occurred likely due to the oxidation of MnO where Mn^{2+} were oxidized into higher oxidation states, *e.g.,* Mn^{3+} and Mn^{4+} (Figures S5c-e and S6). The localized surface plasmon resonance (LSPR) band of Ag NPs appeared at ~ 427 nm when the reaction proceeded for 5 min. Along with increasing reaction time to 30 min, the LSPR band of Ag NPs underwent continuously redshift to ~ 448 nm due to the size increase of Ag NPs from 3.7 ±0.8 to 8.3 ± 1.5 nm. The LSPR band of Ag NPs gradually blue-shifted after 30 min as a result of the change in the uniformity of Ag NPs similar to the observation in previous reports.[41, 42] At 60 min, the further growth of Ag NPs gave rise to a much larger size of 12.0 ± 0.2 nm. Meanwhile, the average size of MnO domains decreased gradually from 14.5 ± 1.1 nm (at 5 min) to 13.5 ± 1.5 nm (at 50 min) along with the growth of Ag domains (Figure S6), suggesting that the growth of Ag NPs induced the oxidative etching of MnO_x domains.
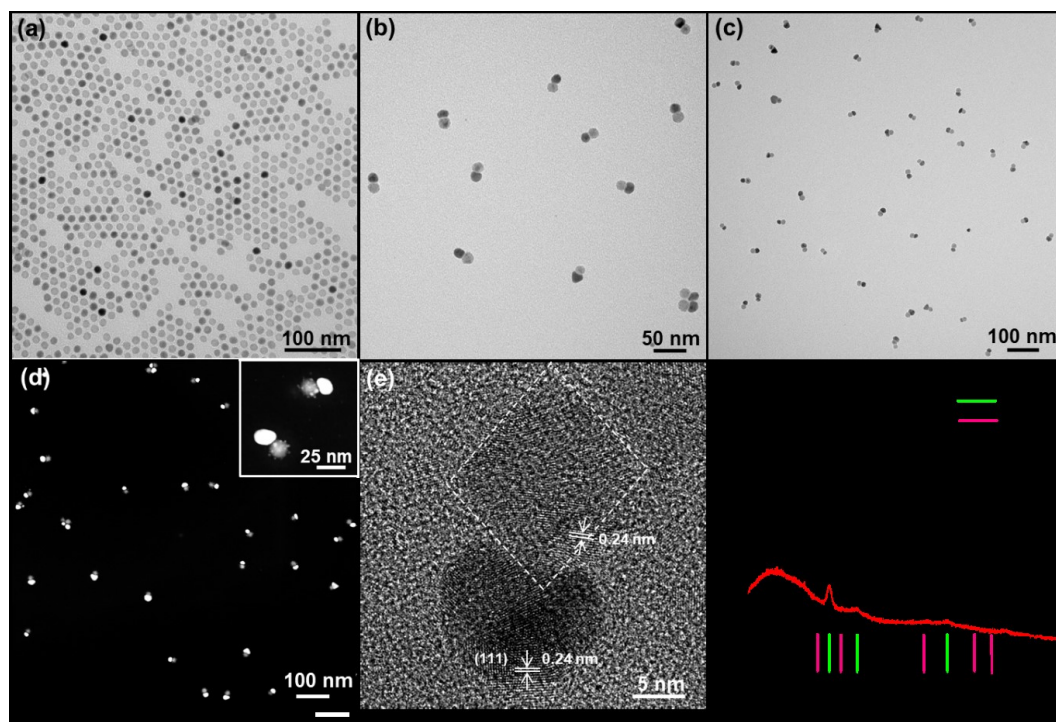
Nanoscale

ARTICLE

Figure 1. The growth and characterizations of Ag domains on MnO octahedra. (a) Low-magnification TEM image of MnO octahedra. (b-c) TEM (d) HAADF–STEM and (e) HR-TEM images of Janus-type MnO_x–Ag NPs. (f) Powder XRD patterns of MnO octahedra (black, top) and MnO_x–Ag (red, bottom). The diffraction peaks for pure Ag and MnO are indicated by vertical lines at the bottom using JCPDF#4-783 and JCPDF#72-783, respectively.

The control of Ag domains can be readily achieved by varying the feeding amount of $AgNO_3$ (Figure S7). When increasing the molar ratio of $AgNO_3$ to MnO from 0.5 to 2, the size of Ag NPs was adjusted from 10.2 ± 1.6 nm to 18.8 ± 2.2 nm (Figure S8). Interestingly, the size of MnO_x decreased from 14.9 ± 0.8 nm to 12.6 ± 1.1 nm accompanied with the size increase of Ag NPs. This further confirms the oxidative growth of Ag when nucleating on MnO octahedra since the etching of MnO_x depends on the content of $AgNO_3$. The growth of Ag on MnO can be further extended by using the ~48 nm of octahedra as template (Figure S9). The formation of core-satellite nanostructures or anisotropic nanostructures with multiple Ag domains can be seen by varying the ratio of $AgNO_3$ to MnO. When the molar ratio of $AgNO_3$ to MnO is low, *e.g.,* 0.25, the formation of small Ag domains (~9.1 nm) was observed preferentially grown at the corners and the edges of MnO octahedra (Figure S10a-b). The core-satellite nanostructures are likely resulted from the limited amount of $AgNO_3$.[43] When the molar ratio $AgNO_3$ to MnO increases to 1, the rate of surface diffusion of Ag is largely enhanced; thus most of Ag domains migrate quickly to the corners of MnO octahedron, leading to the formation of anisotropic nanostructures with multiple Ag domains (1-3 Ag domains per MnO octahedron) (Figure S10c). Anisotropic nanostructures with multiple

Ag domains underwent a blue-shift in the LSPR absorption accompanied with narrowing of the LSPR band compared to that of core-satellite MnO-Ag nanostructures (Figure S10d). This particular blue-shift is presumably caused by the increased distance between Ag NPs due to the decrease dipole-dipole interaction between Ag NPs.[44]

The iodization of Ag domains was carried out at room temperature by mixing Janus-type MnO_x-Ag and CH_3I in hexane. TEM images in Figure 2a shows the uniform MnO_x-AgI NPs in high quality without further size selection (see low-magnification TEM image in Figure S11). The High-resolution TEM (HR-TEM) (Figure 2b) and HAADF-STEM (Figure 2c) images of the resulting Janus MnO_x-AgI NPs were investigated to confirm the existence of AgI. Note that, AgI is sensitive to the electron beam and the focus/alignment cannot be performed on the same NP that was imaged. The Janus MnO_x-AgI NPs consist of MnO_x octahedron with a core-shell Ag-AgI domain where a darker and brighter contrast is from irregular AgI and Ag (see the inset in Figure 2c), respectively. The Ag-AgI domain is clearly core-shell with a shell of AgI ($d = 0.27$ nm of (102) planes) grown on the core of Ag NP ($d = 0.24$ nm of (111) planes) in the HR-TEM image (Figure 2b). To simplify the abbreviation, we use Janus MnO_x-AgI to denote the nanostructures

after iodization, despite of the core-shell Ag@AgI. The boundary between Ag and AgI is unambiguous, suggesting the partial iodization of Ag into AgI. It is interesting to point out that, the small Ag grains (~1 nm) disappeared. The migration of small Ag grains to form dominant AgI NPs tends to minimize the interface of AgI and MnO_x. The size of AgI domains increased to 14.6 ± 2.5 nm (Figure S4b) compared to the original Ag NP (12.0 ± 2.2 nm); while, MnO_x octahedra remained unchanged. The effective iodization of Ag NPs was further studied by UV-Vis spectroscopy. The initial Ag NPs of Janus MnO_x-Ag NPs display a UV absorption peak at ~427 nm (Figure 2d), ascribed to the LSPR band of Ag. After the iodization of Ag domain, the UV-Vis absorption spectra underwent a gradual blue-shift to ~406 nm due to the formation of AgI, known as the characteristic peak of pure AgI nanocrystals at ~ 400 nm.[45]
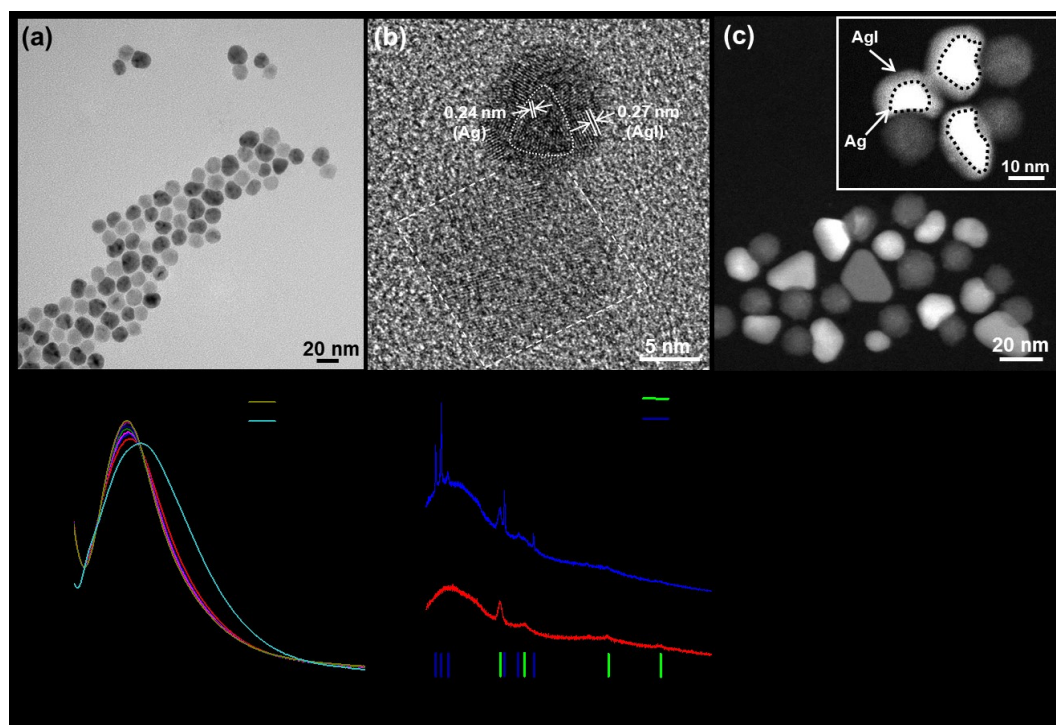

Figure 2. The iodization of Janus-type MnOx-Ag to MnOx-AgI NPs. (a) TEM image, (b) HR-TEM image and (c) HAADF–STEM image of Janus-type MnO_x–AgI NPs. (d) The UV spectra showing the kinetics of the iodization of MnO_x–Ag. The curves were collected at a time interval of 5 min during iodization (from right to left). (e) Powder XRD patterns of Janus-type MnO_x–AgI (blue, top) and the MnO_x–Ag (red, bottom). The diffraction peaks for pure Ag and AgI are indicated by lines given at the bottom using JCPDF #4-783 and JCPDF #3-940, respectively. (f) Corresponding SEM-EDX spectra of as-resultant MnO_x–AgI. The Si and most O peaks are from the substrate.

Powder XRD and energy dispersive X-ray spectroscopy (EDX) were further used to examine the effective of iodization. The XRD pattern (Figure 2e) of Janus-type MnO_x-Ag NPs exhibited the *fcc* crystalline Ag (JCPDF #4-783). After iodization, the XRD feature of AgI (JCPDF #3-940) appeared along with the existing peaks of Ag, implying the co-existing of Ag and AgI. The iodization is incomplete. The SEM-EDX results show that Janus MnO_x-AgI NPs have an atomic ratio of Ag-to-I of 2.4:1 (Figures 2f and S12). It suggests that the conversion of Ag to AgI is *ca*. 42%. All those findings confirm that the iodization of Ag with CH_3I as the sole iodine source is an efficient way to yielding AgI without disrupting the nanostructure of Ag. Compared to other traditional iodine sources such as KI and I_2 (see Figure S13),[46, 47] CH_3I shows a mild iodization rate while preserving the Janus-type nanostructure. In addition, this iodization method is versatile to synthesize Ag@AgI nanocrystals. As our controls, the iodization of spherical Ag NPs with CH_3I shows a similar conversion and controllability (Figure S14). Ag@AgI as a control sample was used to analyze the band gap and energy band as described below.

To understand the change in the oxidation state and chemical nature of MnO_x during synthesis, X-ray photoelectron spectroscopy (XPS) was carried out for MnO octahedra, Janus-type MnO_x–Ag and MnO_x–AgI NPs. The high-resolution spectra of Mn 3s and 2p regions are given in Figure 3a and 3b, respectively (also see Table S1 for details). The peak separation of Mn 3s (ΔE_{3s}) is particularly useful to elucidate the oxidation state of Mn.[20, 26, 29, 48-50] MnO octahedra have a ΔE_{3s} of 5.9 eV, indicating that the oxidation state of Mn is predominantly +2. After the growth of Ag, the ΔE_{3s} of Mn 3s peaks decreases to 5.3 eV, slightly lower than that of Mn_2O_3 (5.5 eV). After iodization, the ΔE_{3s} of Mn 3s peaks further decreases to 5.1 eV. It clearly indicates that MnO_x domains are oxidized for Janus-type MnO_x–Ag and MnO_x–AgI NPs, distinguished from the initial MnO octahedra. Similar results were observed by fitting Mn 2p region (Figure 3b). The binding energy of Mn $2p_{3/2}$ is 640.8 eV for MnO octahedra. It increases to 641.4 eV for MnO_x–Ag and reaches 641.5 eV for MnO_x–AgI Janus nanostructure, implying the increased Mn valence along with the formation of Ag domains.[49, 51, 52] All three samples clearly show a satellite peak at ~647 eV, arising from Mn^{2+} species.[40, 49] Meanwhile, Mn^{3+} and Mn^{4+} species show an

obvious increase in the deconvolution of Mn2p3/2 peak, further indicating the increase in Mn valence during the growth of Ag and AgI (Table S2). Given that the crystallinity of MnOx disappeared in Janus-type MnOx–Ag and MnOx–AgI NPs, it is likely that the nucleation and growth of Ag domains on MnOx induced the oxidation of MnO, resulting in the formation of amorphous MnOx with a mixed valence. In addition, the changes in Ag 3d binding energy of Ag and AgI were investigated to detect the iodization of Ag domain (Figures 3c and S15). The binding energy of Ag 3d5/2 peak exhibited a positive shift and the I 3d peak appeared as the iodization of Ag occurred, revealing the successful formation of AgI.[53]

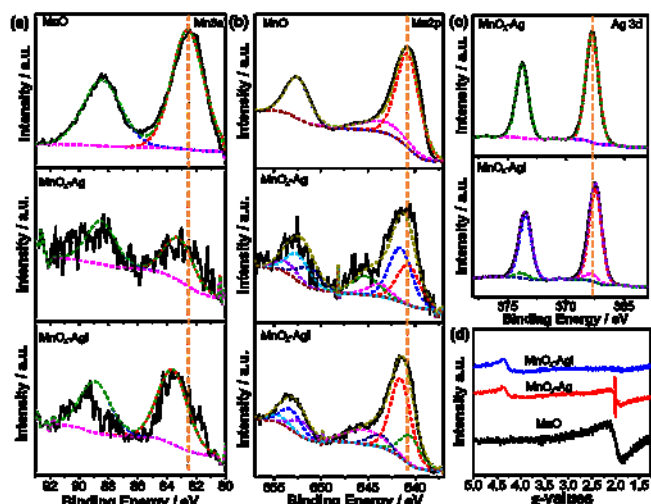
Figure 3. Spectroscopic characterizations of the change in the Mn oxidation states. (a) The fitted Mn 3s peaks of MnO octahedra, Janus-type MnOx–Ag and MnOx–AgI NPs. (b) The Mn 2p deconvoluted results of MnO octahedra, Janus-type MnOx–Ag and MnOx–AgI nanostructures. (c) The Ag 3d fitting results of MnOx–Ag and MnOx–AgI. (d) Perpendicular mode EPR spectra of MnO octahedra (black, bottome), MnOx–Ag (red, middle) and MnOx–AgI (blue, top). EPR spectra were recorded in hexane at room temperature.

Electron paramagnetic resonance (EPR) spectroscopy was further used to confirm the change in the oxidation state of Mn as shown in Figure 3d. A characteristic broad Mn^{2+} signal at g ≈ 2 (S = 5/2) was observed in initial MnO octahedra. For Janus MnOx–Ag and MnOx–AgI nanostructures, a resonance peak at g ≈ 4.35 was seen, assigning to Mn^{4+} (S = 3/2). This is consistent with the analysis of XPS results where the oxidation state of Mn increased accompanied by the oxidative growth of Ag domains. In particular, MnOx–AgI shows Mn species with high oxidation states dominantly since the resonance peak at g ≈ 2 becomes very weak. Note that Mn^{3+} (S = 2) cannot be ruled out from EPR because it was difficult to detect through traditional perpendicular mode of EPR measurement by reason of large zero-field splitting of Mn^{3+}.[48]
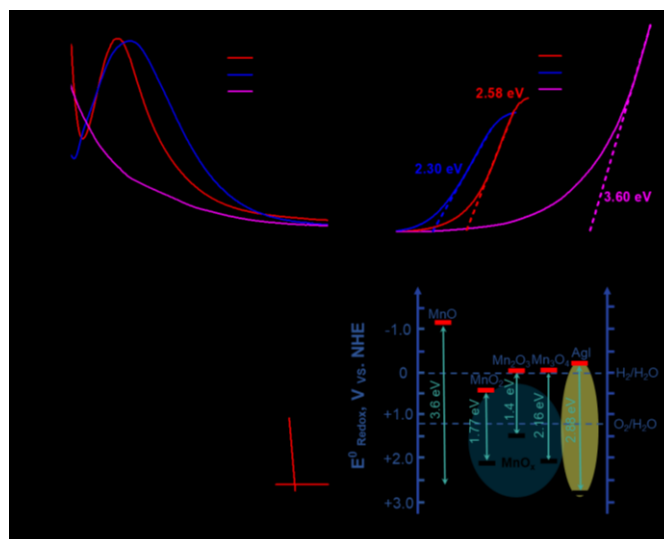

Figure 4. The band gap and electronic analysis of Janus-type MnOx–AgI NPs. (a) The UV-Vis spectra and (b) Tauc plots of AgI (black), MnO octahedra (pink), MnOx-Ag (blue) and MnOx–AgI NPs (red). (c) Valence-band XPS spectrum of AgI NPs. (d) The scheme to show the proposed realignment of the conduction band and valence band of Janus-type MnOx–AgI NPs.

Since MnOx is an *p*-type semiconductor with x > 1.5,[46] coupling *p*-type MnOx with semiconductive AgI likely results in interesting synergies in photocatalysis. We consequently analysed the band energy and band gap of MnOx and AgI using Tauc plot and valence-band XPS spectroscopy. The UV-Vis spectra of AgI, MnO octahedra, Janus-type MnOx–Ag and MnOx–AgI NPs are present in Figure 4a. The sample of AgI was prepared from the iodization of Ag nanospheres directly as described above (see SI for details). The optical bandgap of these samples was estimated using Tauc plot, $\alpha h v = A*(hv-E_g)^\gamma$, where α, *h and v* represent the absorption coefficient, Planck's constant and light frequency, respectively; A is proportionality constant and γ is a constant based on the nature of band gap. Here, γ =2 for indirect transition semiconductor. Figure 4b displays the Tauc plots of $(\alpha h v)^2$ versus phone energy (hv) for the corresponding samples in Figure 4a. Through the linear extrapolation, the band gap of AgI NPs and MnO octahedral was determined to be 2.88 and 3.60, respectively. Moreover, the valence band edge of AgI NPs was measured to be 2.74 eV (relative to *vs.* NHE) by valence-band XPS spectrum of AgI (Figure 4c). Thus, the edge of conduction band and valence band of AgI were calculated to be -0.14 and 2.74 V, respectively. Note that, it was difficult to etch AgI NPs from Janus-type MnOx-AgI without influencing the oxidation states of MnOx. As a result, the accurate band value of MnOx was unable to be determined. Given the mixed valence states of MnOx, the previous reported values of the conduction band edge and valence band edge from MnO, MnO2, Mn2O3 and Mn3O4 were used to estimate the range of band gap in MnOx of the Janus NPs.[54-56] As shown in the Figure 4d, the bandgap of MnOx would become much narrower and the conduction band edge become lower compared to those of original MnO octahedra because of the oxidation of Mn^{2+}.
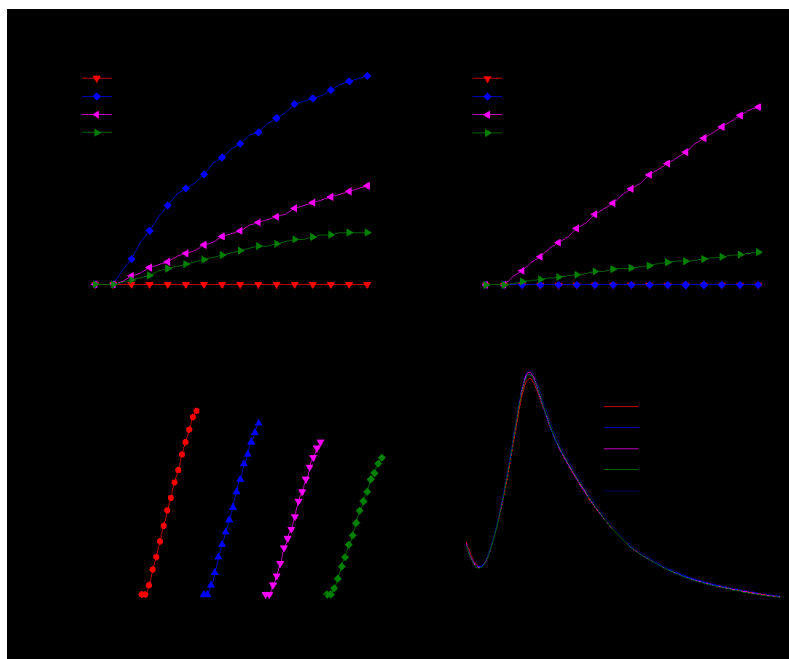
Nanoscale

Figure 5. Photocatalytic performance of catalysts under visible light. Dissolved oxygen evolution profiles for the photochemical water oxidation with (a) and without (b) $Ru(bpy)_3Cl_2$. Photocatalytic conditions: 4 mg of catalysts, 13 mM $Na_2S_2O_8$, and 68 mM Na_2SO_4 in 15 mL of Na_2SiF_6−$NaHCO_3$ buffer with (pH ~5.8). 1.5 mM of $Ru(bpy)_3Cl_2$ was added for the measurements in (a). (c) Stability measurement of Janus-type MnO_x-AgI in consecutive five cycles. (d) The UV-Vis spectra of Janus-type MnO_x-AgI aqueous solution irradiated by visible light up to 5 h.

We further evaluate the catalytic synergies of Janus MnO_x–AgI nanostructures for photochemical WORs. Those Janus NPs were transferred to the aqueous solution using polyvinylpyrrolidone (PVP) as surface ligands. Photochemical water oxidation was firstly performed using the $Ru(bpy)_3Cl_2$/$Na_2S_2O_8$ system in a Na_2SiF_6−$NaHCO_3$ buffer (pH ~5.8). The reaction was irradiated using a halogen lamp with a cutoff filter (λ > 400 ± 10 nm, light intensity 1 w/cm^2). The amount of dissolved oxygen was measured using an automatic temperature-compensated handheld oxygen microsensor (Seven2GoTM portable DO Meter). The catalytic results are summarized in Figure 5a. Janus MnO_x-AgI NPs displayed a superior activity for photocatalytic WORs. The dissolved oxygen concentration quickly increased to 87 mmol per $mg_{catalyst}$ after irradiation for 280 s (same for other samples). This result is comparable to the active Mn_2O_3 photocatalysts.[50] Although AgI solely is active for photocatalytic WORs as well, Janus MnO_x-AgI NPs are 4 times more active than AgI. In addition, the MnO exhibited a negligible amount of oxygen evolution. It is interesting to point out that Janus MnO_x-Ag NPs were active for oxygen evolution. This suggests that the mixed valence states of MnO_x with Mn^{3+} and Mn^{4+} are the active species for water oxidation.

Since integrating AgI with MnO_x significantly enhanced the photocatalytic activity, we further examined visible light-driven water oxidation of Janus MnO_x-AgI NPs without $Ru(bpy)_3^{2+}$ to understand the synergies between AgI with MnO_x. It is remarkable that Janus MnO_x-AgI NPs produced 74 mmol O_2 per $mg_{catalyst}$ under identical conditions but without $Ru(bpy)_3Cl_2$ as an electron mediator (Figure 5b). This suggests that Janus-type MnO_x-AgI NPs are efficient photocatalysts with minimized dependence on the presence of $Ru(bpy)_3Cl_2$ for WORs. AgI NPs exclusively produced 14 mmol O_2, comparable to that of AgI NPs with $Ru(bpy)_3Cl_2$ (21 mmol O_2). While in the absence of $Ru(bpy)_3Cl_2$, both MnO_x-Ag and MnO are inactive for photocatalytic WORs.

In a traditional photocatalytic system with a sole *p*-type MnO_x, the $Ru(bpy)_3^{3+}$/$Ru(bpy)_3^{2+}$ pair act as electron shuttles to facilitate the charge separation on the photocatalyst, *e.g.,* MnO_x (Figure S16). When coupling AgI with MnO_x directly in a Janus-type topology, AgI has an indirect bandgap of 2.4-2.6 eV. Although AgI solely is active, Janus-type MnO_x-AgI shows much better activity for water oxidation. On contrary, when physically mixing MnO and AgI, no improvement in activity was found (see Figure S17).

In the absence of $Ru(bpy)_3Cl_2$, since the MnO_x-Ag becomes inactive, the electron excitation occurring on the MnO_x domain cannot be utilized because of the lack of charge separation. The photogenerated holes on AgI can still oxidize water as observed in Figure 5b. When coupled with MnO_x in the absence of $Ru(bpy)_3Cl_2$,

there is a 5-times increase in activity. This suggests that the amorphous MnO_x can presumably work as a hole transporter[57] to separate the photoexcited hole from AgI. Furthermore, it is noteworthy that Janus-type MnO_x-AgI is active for solar-driven WORs without Na_2SiF_6−$NaHCO_3$ buffer as well (see Figure S18). This is indicative of the satisfactory tolerance of acidity for Janus MnO_x-AgI photocatalyst.

AgI is extremely photosensitive.[53, 58, 59] Upon excitation by light, I^- ions can be oxidized into I_2 to generate reductive electrons in the conduction band of AgI; while, Ag^+ ions can be photoreduced to metallic Ag. To assess the durability of Janus-type MnO_x-AgI photocatalyst, the light-driven WORs of MnO_x-AgI were measured repeatedly by recovering the photocatalyst after the reactions. As shown in Figure 5c, Janus MnO_x-AgI photocatalyst can maintain O_2 production rate with a slight decrease in its activity. After five cycles, a retention of 69% of its initial activity was received. We further used XRD and EPR to investigate the photostability of MnO_x-AgI after five cycles. The crystallinity of Janus NPs and the oxidative state of Mn remained unchanged (Figures S19a-S20). The nanostructural integrity of MnO_x-AgI was also confirmed by TEM where Janus nanostructures were well-preserved (Figure S19b-c). To further validate the photostability of AgI domains, we have collected the UV-Vis spectra of the MnO_x-AgI aqueous solution under visible light for 5 h.[60] The maximum absorbance at its absorption peak is substantially unchanged during photoirradiation (Figure 5d). As suggested by the recent studies from Sun *et al*., AgI can be stabilized in the presence of plasmonic Ag nanoparticles (NPs, Ag@AgI NPs) with the polarized plasmonic field of Ag.[60, 61]

Conclusions

To summarize, we reported a new synthetic approach to growing two Janus-type MnO_x-Ag and MnO_x-AgI NPs on MnO octahedra via the oxidative nucleation and growth method. A mild iodization technique was developed to convert Ag to AgI with CH_3I as the sole iodide source; so that Janus-type MnO_x-Ag NPs could be converted to MnO_x-AgI NPs without the disruption of their nanostructures. The oxidation of MnO was observed to form mixed amorphous MnO_x in the course of the growth of Ag domains and the formation of AgI domains. The MnO_x-AgI NPs as photocatalysts proved to be highly active under visible light irradiation in the absence of $Ru(bpy)_3Cl_2$ an electron mediator. The marriage of MnO_x and AgI brings the synergies to separate the photoexcited holes to largely enhance the photocatalytic active, compared to pure MnO_x and AgI. Our studies therefore not only open a new avenue to develop MnO_x-containing asymmetric nanostructures, but also illustrate a new pathway to design photocatalysts that potentially show high charge separation efficiency.

Experimental Section

Chemicals and Materials.

Manganese(II) chloride tetrahydrate (> 98 %), 1-ocdacene (90 %), oleic acid (90 %), methanol (≥ 99.9 %), sodium hydroxide (95 %), acetone (≥ 99.9 %), hexane (≥ 98.5 %), oleylamine (70%), 4-*tert*-

butyl toluene (95%), sodium persulfate (>98%), sodium sulfate (anhydrous, >99%), sodium hexafluorosilicate, tetrahydrofuran(≥ 99 %), polyvinylpyrrolidone (M_w=40000) and sodium bicarbonate (>99.5%) were purchased from Sigma-Aldrich and used as received otherwise noted. Silver nitrate (≥ 99 %) was obtained by Aldrich Chem. Inc. Iodomethane (99 %, stable with copper) was purchased from Alfa Aesar. Tris(2,2-bipyridyl) ruthenium (II) chloride hexahydrate [$Ru(bpy)_3^{2+}$] (98%) was obtained by Acros Organic. The ultra-pure water was obtained using High-Q, Inc. system (model 103S).

Synthesis of Mn(oleate)₂ precursor.

$Mn(oleate)_2$ was prepared according to the previous report.[62] Typically, 7.92 g of $MnCl_2·4H_2O$ (0.06 mol) and 22.6 g oleic acid (0.08 mol) were totally dissolved in 200 mL of methanol. Then, a methanol solution containing 3.2 g NaOH was dropped slowly into above mixture under intensely stirring. After stirring for 2 h, the brown precipitate was collected by filtration and followed by washing with methanol and drying under vacuum.

Synthesis of MnO octahedra with different sizes.

In a typical synthesis of MnO octahedron, 6.2 g of $Mn(oleate)_2$ (0.01 mol), 6.21 g of oleic acid (0.02 mol) and 50 g 1-ocdacene were mixed in a 100 mL three-necked flask equipped with a condenser. The reaction mixture was heated to 80 °C under nitrogen atmosphere. The reaction mixture was then vacuumed for 1 h to completely remove residual water and dissolved air. The temperature was further increased to 320 °C at a rate of 7 °C/min. The color gradually changed from orange to green suspension when temperature reached at 320 °C. Then, the mixture was stirred for another 1 h before it was cooled down to room temperature. Finally, the product was collected by precipitating with excess acetone and washing with hexane. The collected product was redispersed and stored in hexane with a concentration of 20 mg/mL. The concentration of NPs was determined by drying 500 μL of MnO octahedra in hexane under N_2 and weighted. The size of MnO octahedra determined by electron microscopy is 15.1 ± 0.1 nm. MnO octahedra with various sizes can be obtained by tuning the heating rate as reported previously.[40]

Synthesis of Janus-type MnOₓ-Ag NPs.

A solution of $AgNO_3$ in oleylamine (50 mg/mL) was first prepared. In a typical synthesis of MnO_x-Ag, 1 mL of $AgNO_3$ (50 mg/mL), 1 mL of MnO (20 mg/mL) were added into 4-*tert*-butyl toluene (50 mL) at room temperature. The solution was then stirred at room temperature for 30 min; it was then heated to 110 °C at heating rate of 5 °C/min and further reacted for 1 h. The resulting NPs were collected by centrifugation at 6000 rpm. The final sample was stored in 10 mL of hexane.

Synthesis of Janus-type MnOₓ-AgI NPs.

100 μL of oleic acid was added into 5 mL of as-prepared MnO_x-Ag NPs (5 mg/mL) in hexane under stirring. 300 μL of iodomethane was added dropwise into the above mixture at room temperature. The solution was incubated at room temperature for 30 min. The resulting MnO_x-AgI Janus nanostructure was collected by centrifugation at 6000 rpm.

Synthesis of spherical Ag and Ag@AgI NPs.

11 nm of Ag nanospheres was synthesized by using a reported procedure by Sun *et al.*[63] Briefly, 50 mg of $AgNO_3$ was dissolved in 5.9 mL oleylamine at 60 °C and then heated to 180 °C for 1 h under nitrogen. The resulting Ag nanospheres was obtained by centrifugation at 9000 rpm/10 min and redispersed in 10 mL of hexane with a concentration of 3 mg/mL. The concentration of Ag nanospheres was obtained by drying 500 μl of Ag nanospheres in hexane under N_2 and weighed. The iodization of Ag nanospheres was carried out using a similar procedure as described for Janus-type MnO_x-AgI NPs.

Photochemical water oxidation reaction.

All the catalysts obtained in oil phase were first transferred to the aqueous solution using polyvinylpyrrolidone (PVP) as surface ligands. In a typical transfer process, 5 mL MnO_x-AgI (5mg/ mL) NPs in hexane was centrifuged and then dispersed in the solution of 5 ml THF containing 100 mg of PVP (M_w = 40000). After heating above mixture at 75 °C for 6 min, PVP dissolved in the hot THF and stabilized the catalyst. Then cooling down the mixture to room temperature, the aqueous solution of catalyst was finally obtained by collecting the precipitation and then redispersed it in the water. The aqueous solution of catalyst was washed 5 times to remove the excess surface ligand before photocatalytic test. The concentration of catalyst was confirmed by centrifuging and drying them in oven as well as weighted. Typically, photochemical water oxidation tests were performed in a 25 mL sealed quartz reaction vessel containing 4 mg of catalyst, 13 mM of $Na_2S_2O_8$, and 68 mM of Na_2SO_4 in 15 mL of buffered aqueous solutions (0.025 M Na_2SiF_6−$NaHCO_3$ solution at pH~5.8). 1.5 mM of Ru(bpy)$_3$Cl$_2$ was added for the measurements in Figure 5a. Reactants in the quartz vessel were sonicated and purged with nitrogen for 10 min to remove all dissolved oxygen from the aqueous solution. The quartz vessel was then irradiated with a continuous output halogen lamp (150 W). A cutoff filter (λ > 400 ± 10 nm, SCHOTT North America, Inc.) was placed on the light source to remove UV light. Light intensity at the sample was measured to be 1 W cm^{-2}, using digital light meter (LX1330B). The perpendicular distance between light source and reaction quartz vessel was fixed to be 3.5 cm. The amount of dissolved oxygen was measured using an automatic temperature-compensated handheld oxygen microsensor (Seven2GoTM pro DO Meter). The photochemical water oxidation measurements of Janus-type MnO_x-AgI nanostructure and Ag nanospheres were conducted following a similar procedure except without Ru(bpy)$_3$$^{2+}$.For stability test of Janus-type MnO_x-AgI NPs, the visible light driven water oxidation of MnO-AgI NPs was repeating 5 times by using the same catalyst recovered from the previous cycle through centrifugation.

Characterizations.

HR-TEM and HAADF-STEM image were performed by using FEI Talos F200X Atomic Resolution Analytical Microscope. TEM was carried out on FEI Tecnai 12 G2 Spirit BioTWIN. The TEM samples were prepared by dropping the solution of sample on the carbon-coated copper grids (400 mesh). The size distribution of sample was obtained by calculating at least 300 particles ffrom low-magnification TEM images through Nano measure software. SEM images and energy disperse X-ray spectroscopy (EDS) were recorded by a FEI Nova NanoSEM 450. XRD patterns were recorded by using a Rigaku Ultima IV diffractometer equipped with graphite-monochromatized Cu Kα radiation in *2θ* ranging from 10º to 90º at scan rate of 0.5°/min. EPR spectroscopy was carried out on a Bruker EMX CW-microspectrometer with traditional perpendicular mode (samples dispersed in hexane) at room temperature. The pH value was measured by pH tester of HANNA instrument (H198103). The PH tester was calibrated by two-point pH buffer before use. XPS were performed on a PHI Quantum 2000 spectrometer with a multiprobe (Physical Electronics Industries Inc) that uses Al Kα radiation. The binding energy of the C 1s peak (284.6 eV) was employed as a standard to calibrate the binding energies of other elements.

Conflicts of interest

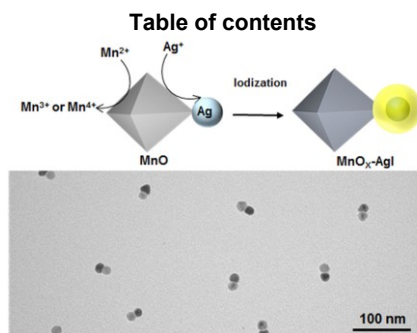There are no conflicts to declare.

Acknowledgements

References

1. R. Costi, A. E. Saunders and U. Banin, *Angew. Chem. Int. Ed.*, 2010, **49**, 4878-4897.
2. R. Ghosh Chaudhuri and S. Paria, *Chem. Rev*, 2011, **112**, 2373-2433.
3. M. B. Gawande, A. Goswami, T. Asefa, H. Guo, A. V. Biradar, D.-L. Peng, R. Zboril and R. S. Varma, *Chem. Soc. Rev.*, 2015, **44**, 7540-7590.
4. D. J. Milliron, S. M. Hughes, Y. Cui, L. Manna, J. Li, L.-W. Wang and A. P. Alivisatos, *Nature*, 2004, **430**, 190.
5. D. Deng, K. Novoselov, Q. Fu, N. Zheng, Z. Tian and X. Bao, *Nature Nanotech.*, 2016, **11**, 218.
6. R. Ferrando, J. Jellinek and R. L. Johnston, *Chem. Rev*, 2008, **108**, 845-910.
7. H. You, S. Yang, B. Ding and H. Yang, *Chem. Soc. Rev.*, 2013, **42**, 2880-2904.
8. Y. Sun, *Natl. Sci. Rev.*, 2015, **2**, 329-348.
9. A. Walther and A. H. Müller, *Chem. Rev*, 2013, **113**, 5194-5261.
10. J. He, Y. Liu, T. C. Hood, P. Zhang, J. Gong and Z. Nie, *Nanoscale*, 2013, **5**, 5151-5166.

ARTICLE

11. T. Yang, L. Wei, L. Jing, J. Liang, X. Zhang, M. Tang, M. J. Monteiro, Y. Chen, Y. Wang and S. Gu, *Angew. Chem. Int. Ed.*, 2017, **56**, 8459-8463.

12. Z. W. Seh, S. Liu, M. Low, S. Y. Zhang, Z. Liu, A. Mlayah and M. Y. Han, *Adv. Mater.*, 2012, **24**, 2310-2314.

13. S. K. Cushing, J. Li, F. Meng, T. R. Senty, S. Suri, M. Zhi, M. Li, A. D. Bristow and N. Wu, *J. Am. Chem. Soc.*, 2012, **134**, 15033-15041.

14. P. Li, Z. Wei, T. Wu, Q. Peng and Y. Li, *J. Am. Chem. Soc.*, 2011, **133**, 5660-5663.

15. M. N. Tahir, F. Natalio, M. A. Cambaz, M. Panthöfer, R. Branscheid, U. Kolb and W. Tremel, *Nanoscale*, 2013, **5**, 9944-9949.

16. Q. Yuan, D. Liu, N. Zhang, W. Ye, H. Ju, L. Shi, R. Long, J. Zhu and Y. Xiong, *Angew. Chem. Int. Ed.*, 2017, **129**, 4270-4274.

17. J. Guo, Q. Liu, C. Wang and M. R. Zachariah, *Adv. Funct. Mater.*, 2012, **22**, 803-811.

18. K. L. Pickrahn, S. W. Park, Y. Gorlin, H.-B.-R. Lee, T. F. Jaramillo and S. F. Bent, *Adv. Energy. Mater.*, 2012, **2**, 1269-1277.

19. R. Frydendal, E. A. Paoli, I. Chorkendorff, J. Rossmeisl and I. E. L. Stephens, *Adv. Energy. Mater.*, 2015, **5**, 1500991.

20. D. Jeong, K. Jin, S. E. Jerng, H. Seo, D. Kim, S. H. Nahm, S. H. Kim and K. T. Nam, *ACS Catal.*, 2015, **5**, 4624-4628.

21. P. F. Smith, B. J. Deibert, S. Kaushik, G. Gardner, S. Hwang, H. Wang, J. F. Al-Sharab, E. Garfunkel, L. Fabris, J. Li and G. C. Dismukes, *ACS Catal.*, 2016, **6**, 2089-2099.

22. B. Liu, I. M. Mosa, W. Song, H. Zheng, C.-H. Kuo, J. F. Rusling, S. L. Suib and J. He, *J. Mater. Chem. A*, 2016, **4**, 6447-6455.

23. F. Zhou, A. Izgorodin, R. K. Hocking, L. Spiccia and D. R. MacFarlane, *Adv. Energy. Mater.*, 2012, **2**, 1013-1021.

24. Y.-F. Li and Z.-P. Liu, *J. Am. Chem. Soc.*, 2018, **140**, 1783-1792.

25. F. Jiao and H. Frei, *Chem. Commun.*, 2010, **46**, 2920-2922.

26. D. M. Robinson, Y. B. Go, M. Mui, G. Gardner, Z. Zhang, D. Mastrogiovanni, E. Garfunkel, J. Li, M. Greenblatt and G. C. Dismukes, *J. Am. Chem. Soc.*, 2013, **135**, 3494-3501.

27. F. Cheng, T. Zhang, Y. Zhang, J. Du, X. Han and J. Chen, *Angew. Chem. Int. Ed.*, 2013, **52**, 2474-2477.

28. T. Takashima, K. Hashimoto and R. Nakamura, *J. Am. Chem. Soc.*, 2012, **134**, 1519-1527.

29. A. Iyer, J. Del-Pilar, C. K. King'ondu, E. Kissel, H. F. Garces, H. Huang, A. M. El-Sawy, P. K. Dutta and S. L. Suib, *J. Phys. Chem. C*, 2012, **116**, 6474-6483.

30. B. A. Pinaud, Z. Chen, D. N. Abram and T. F. Jaramillo, *J. Phys. Chem. C*, 2011, **115**, 11830-11838.

31. D. Hong, Y. Yamada, T. Nagatomi, Y. Takai and S. Fukuzumi, *J. Am. Chem. Soc.*, 2012, **134**, 19572-19575.

32. H. Zhu, A. Sigdel, S. Zhang, D. Su, Z. Xi, Q. Li and S. Sun, *Angew. Chem. Int. Ed.*, 2014, **126**, 12716-12720.

33. H. T. Tan, X. Rui, Z. Lu, C. Xu, W. Liu, H. H. Hng and Q. Yan, *J. Phys. Chem. C*, 2014, **118**, 17452-17460.

34. I. Schick, S. Lorenz, D. Gehrig, A.-M. Schilmann, H. Bauer, M. Panthöfer, K. Fischer, D. Strand, F. Laquai and W. Tremel, *J. Am. Chem. Soc.*, 2014, **136**, 2473-2483.

35. D. Shin, Y. Park, H. Ryu, W. S. Seo and H. Song, *CrystEngComm*, 2016, **18**, 4188-4195.

36. H. Zhu, A. Sigdel, S. Zhang, D. Su, Z. Xi, Q. Li and S. Sun, *Angewandte Chemie*, 2014, **126**, 12716-12720.

37. J. Zeng, M. Li, A. Liu, F. Feng, T. Zeng, W. Duan, M. Li, M. Gong, C.-Y. Wen and Y. Yin, *Adv. Funct. Mater.*, 2018, **28**, 1800515.

38. R. Makiura, T. Yonemura, T. Yamada, M. Yamauchi, R. Ikeda, H. Kitagawa, K. Kato and M. Takata, *Nat. Mater.*, 2009, **8**, 476-480.

39. J. Park, K. An, Y. Hwang, J. G. Park, H. J. Noh, J. Y. Kim, J. H. Park, N. M. Hwang and T. Hyeon, *Nat. Mater.*, 2004, **3**, 891-895.

40. C. H. Kuo, I. M. Mosa, S. Thanneeru, V. Sharma, L. Zhang, S. Biswas, M. Aindow, S. Pamir Alpay, J. F. Rusling, S. L. Suib and J. He, *Chem. Commun.*, 2015, **51**, 5951-5954.

41. D. Mott, N. T. Thuy, Y. Aoki and S. Maenosono, *Philos. Trans. A. Math. Phys. Eng. Sci.*, 2010, **368**, 4275-4292.

42. J. Yang, B. Cao and B. Liu, *Mater. Res. Express.*, 2014, **1**, 015022.

43. X. Xia, S. Xie, M. Liu, H. C. Peng, N. Lu, J. Wang, M. J. Kim and Y. Xia, *Proc. Natl. Acad. Sci. U.S.A.*, 2013, **110**, 6669-6673.

44. F. Otieno, M. Airo, K. Ranganathan and D. Wamwangi, *Thin Solid Films*, 2016, **598**, 177-183.

45. L. Zhang, T. Liu, K. Liu, L. Han, Y. Yin and C. Gao, *Nano Lett*, 2015, **15**, 4448-4454.

46. X. Xia, H. Li and Z. H. Chen, *J. Electrochem. Soc.*, 1989, **136**, 266-271.

47. I. Rivas, D. Puente, I. Ayerdi and E. Castano, 2005.

48. A. Indra, P. W. Menezes, I. Zaharieva, E. Baktash, J. Pfrommer, M. Schwarze, H. Dau and M. Driess, *Angew. Chem. Int. Ed.*, 2013, **52**, 13206-13210.

49. M. C. Biesinger, B. P. Payne, A. P. Grosvenor, L. W. M. Lau, A. R. Gerson and R. S. C. Smart, *Appl. Surf. Sci.*, 2011, **257**, 2717-2730.

50. C.-H. Kuo, I. M. Mosa, A. S. Poyraz, S. Biswas, A. M. El-Sawy, W. Song, Z. Luo, S.-Y. Chen, J. F. Rusling, J. He and S. L. Suib, *ACS Catal.*, 2015, **5**, 1693-1699.

51. J. M. Cerrato, M. F. Hochella, W. R. Knocke, A. M. Dietrich and T. F. Cromer, *Environ. Sci. Technol.*, 2010, **44**, 5881-5886.

52. H. W. Nesbitt and D. Banerjee, *Am. Mineral.*, 1998, **83**, 305-315.

53. M. U. Khan, H. You, X. Liu, L. Zhang and J. Fang, *Small*, 2018, **14**.

54. A. Ginsburg, D. A. Keller, H.-N. Barad, K. Rietwyk, Y. Bouhadana, A. Anderson and A. Zaban, *Thin Solid Films*, 2016, **615**, 261-264.

55. Q. Ma, H. Wang, H. Zhang, X. Cheng, M. Xie and Q. Cheng, *Sep. Purif. Technol.*, 2017, **189**, 193-203.

56. J. Zhao, Z. Zhao, N. Li, J. Nan, R. Yu and J. Du, *Chem. Eng. J.*, 2018, **353**, 805-813.

57. D. K. Kanan and E. A. Carter, *J. Mater. Chem. A*, 2013, **1**, 9246.

58. H. Yu, L. Liu, X. Wang, P. Wang, J. Yu and Y. Wang, *Dalton Trans.*, 2012, **41**, 10405-10411.

59. W. Xie and S. Schlucker, *Nat. Commun.*, 2015, **6**, 7570.

60. C. An, J. Wang, J. Liu, S. Wang and Y. Sun, *ChemSusChem*, 2013, **6**, 1931-1937.

61. C. An, S. Wang, Y. Sun, Q. Zhang, J. Zhang, C. Wang and J. Fang, *J. Mater. Chem. A*, 2016, **4**, 4336-4352.

62. N. R. Jana, Y. Chen and X. Peng, *Chem. Mater*, 2004, **16**, 3931-3935.

63. S. Peng, J. M. McMahon, G. C. Schatz, S. K. Gray and Y. Sun, *Proc. Natl. Acad. Sci. U.S.A.*, 2010, **107**, 14530.

Table of contents

We report a novel synthetic method of Janus-type MnO_x-Ag and MnO_x-AgI nanoparticles based on oxidative nucleation and growth.